Cellulose
https://doi.org/10.1007/s10570-025-06429-7

ORIGINAL RESEARCH

Dual-functionality of *Hibiscus sabdariffa*-CuO nanoparticles in chemotherapy and textile screen-printing on cellulose-based textiles

Elif Tüzün · Ayşe Erol · Ferdane Danışman Kalındemirtaş · Fatih Özbaş · Esra Sert · Razium Ali Soomro · Ayman Nafady · Selcan Karakuş

Received: 3 November 2024 / Accepted: 3 February 2025

Abstract The dual-functional nanostructures show great promise for biomedical applications, exhibiting selective cytotoxicity against cancer cells while also serving as a crucial component in textile screen-printing for smart materials. In this study, we successfully synthesized polyethylene glycol-hibiscus extract copper (II) oxide nanoparticles (PEG/HS/CuO NPs) using a simple one-step sonosynthesis method that leverages ultrasonic irradiation. Comprehensive characterization of the synthesized PEG/HS/CuO NPs was performed using transmission electron microscopy (TEM), X-ray diffraction (XRD), scanning electron microscopy (SEM) coupled with energy-dispersive X-ray (EDX) analysis, and Fourier-transform infrared spectroscopy (FTIR). The incorporation of PEG/HS/CuO NPs into guar gum photochromic solution (GP) caused a significant color change after 6 ± 1 min of UV light exposure and resulted in visible coloration on cellulose-based textiles after screen printing, providing an alternative strategy for smart fabrics. Moreover, cytotoxicity experiments demonstrated the selective toxicity of green PEG/HS/CuO NPs against cancer cells. In this study, the human colon cancer cell line HCT116, breast cancer cell line MCF-7, and normal HUVEC cells were examined. PEG/HS/CuO NPs NPs induced apoptosis, cell cycle arrest, and down-regulation of CD44 antibody expression in MCF-7 cells, highlighting their potential as effective chemotherapy agents.

Supplementary Information The online version contains supplementary material available at https://doi.org/10.1007/s10570-025-06429-7.

E. Tüzün · S. Karakuş (✉)
Department of Chemistry, Faculty of Engineering, Istanbul University-Cerrahpaşa, 34320 Istanbul, Turkey
e-mail: selcan@iuc.edu.tr

A. Erol
Department of Medical Biology, Istanbul Faculty of Medicine, Istanbul University, Istanbul 34104, Turkey

F. D. Kalındemirtaş
Department of Physiology, Faculty of Medicine, Erzincan Binali Yildirim University, 24100 Erzincan, Turkey

F. Özbaş
Department of Restoration and Conservation of Cultural Assets, Faculty of Arts, Design and Architecture, Fatih Sultan Mehmet Vakif University, 34015 Istanbul, Turkey

E. Sert
Department of Hematology, Istanbul Faculty of Medicine, Istanbul University, 34104 Istanbul, Turkey

R. A. Soomro
State Key Laboratory of Organic-Inorganic Composites, Beijing Key Laboratory of Electrochemical Process and Technology for Materials, Beijing University of Chemical Technology, Beijing 100029, China

A. Nafady
Department of Chemistry, College of Science, King Saud University, 11451 Riyadh, Saudi Arabia

S. Karakuş
Health Biotechnology Joint Research and Application Center of Excellence, 34220 Esenler, Istanbul, Turkey

Published online: 11 February 2025

Keywords Screen printing · Apoptosis · Copper (II) oxide nanoparticles · MCF-7 · Cellulose-based textiles

Introduction

The demand for multifunctional textile nanomaterials, driven by technological advancements, arises from the expectation of improving quality of life, harnessing economic potential, enhancing energy efficiency, embracing eco-friendly perspectives, and addressing a variety of needs (Wan et al. 2023; dos Santos et al. 2023). These nanoformulations are accelerating the development of innovative and sustainable products in the textile industry, providing users with multifunctional and eco-conscious solutions. Photocromic, fluorescent, superhydrophobic, antibacterial, antifungal, anticancer, and self-cleaning properties are key characteristics of multifunctional textile materials (Zheng et al. 2024). These properties enhance the advanced roles and versatility of textile products in various technical and biomedical applications. The growing interest in environmentally friendly solutions has driven manufacturers to adopt innovative methods to increase the use of green textile nanomaterials. This reflects the industry's commitment to sustainability and its pursuit of environmentally sound products. Light-sensitive photochromic materials are a key component of smart textiles. Photochromism, a phenomenon involving light-induced color transitions between two distinct optical states, enhances the visual appeal of textile products while enabling users to adapt to changing environmental conditions. Photochromic materials have been applied in various fields, including sunglasses, detectors, displays, memory devices, packaging, optics, and personal care products. It has also aided in the creation of visually appealing traffic and road signs and advertising. Photochromic textile fibers have the ability to change color when exposed to visible light or UV rays. However, the dyes usually degrade during coloring, reducing absorption and diffusion between the fibers (Alsharief et al. 2022).

The functionalization of polymer-based paints and inks with micron- and nano-sized particles has led to significant advancements in developing textile-based products and sensors. These materials can be seamlessly integrated into textiles through various printing techniques (Andra et al. 2021; Hu et al. 2024; Zhang et al. 2024; Zheng et al. 2024). Nonetheless, the current limitations associated with this methodology relate to the challenges in controlling the dispersion and even distribution of additives inside the ink, the reproducibility of product features, process reliability, and cytotoxicity of both the method and structures. In fact, with careful adaption and design of multifunctional features, textiles can offer much more than the sensing capabilities realized by typical sensor integration. Consumers will profit greatly from the approach since it has anticancer properties in addition to minimal toxicity. In addition to promoting skin health in cancer patients, anticancer textiles lower the risk of infection and enhance general health. These textiles are also composed of soft, light, and breathable components, which improve patient comfort during treatment, and they include cell-repairing characteristics that encourage regeneration of the skin. Anticancer textiles, therefore, hold promise for improving the quality of life of cancer patients both mentally and physically. For example, Marra et al. developed smart textile strain sensors consisting of graphene nanoplatelet-based ink, fully integrated using a screen printing technique (Marra et al. 2021). In another study, Yang et al. developed high-performance flexible planar micro-supercapacitors using screen-printed electrodes composed of molybdenum disulfide nanoparticles (MoS_2 NPs) decorated on electrochemically exfoliated graphene. These micro-supercapacitors exhibited excellent flexibility, cycling stability, and remarkable area-specific capacitance, highlighting their highly integrated functionality (Yang et al. 2022). According to the study by Shahzadi et al. (2024), a composite material of polyurethane and strontium aluminate ($SrAl_2O_4$) doped with europium (Eu^{2+}) and dysprosium (Dy^{3+}) demonstrated long-persistent phosphorescence when activated at room temperature, making it suitable for textile-based applications (Shahzadi et al. 2024).

Hibiscus sabdariffa (commonly known as red sorrel or roselle), renowned for its distinctive morphology, is extensively cultivated in many developing nations. This plant is characterized by its deeply lobed leaves, reddish stems, and vibrant calyces, which are widely used for various applications. Over 300 species of hibiscus are found in tropical and subtropical regions worldwide. Hibiscus plants are originally native to areas stretching from India to

Malaysia (Riaz and Chopra 2018). The genus Hibiscus includes more than 250 species of shrubs, trees, and herbs, which are distributed across tropical and subtropical regions. Plants in this genus are known to contain bioactive compounds such as flavonoids, alkaloids, and tannins, which are associated with various health benefits. These compounds are believed to contribute to the plants' anticancer, antioxidant, and antimicrobial properties. Hibiscus contains bioactive substances capable of neutralizing harmful free radicals, thereby mitigating oxidative stress and inflammation (Marques Mandaji et al. 2022). Some research suggests that hibiscus extracts may have anti-inflammatory properties, potentially aiding in the reduction of inflammation. Hibiscus has also been studied for its potential to lower cholesterol levels and blood pressure, which can reduce the risk of heart disease. Additionally, hibiscus extracts have been shown to inhibit the growth of certain cancer cell lines in vitro, though further research is needed to confirm these effects. There is also evidence that hibiscus extracts may help protect the liver from damage caused by toxins or diseases.

Cancer presents a significant challenge in the domain of global public health, marked by the uncontrolled proliferation of abnormal cells, culminating in severe ramifications. Projections indicate a troubling scenario, with an anticipated surge to approximately 2.6 million new cancer cases annually by the year 2030, accompanied by an estimated 1.7 million fatalities per year. Notably acknowledged by the World Health Organization (WHO), prominent cancer types encompass breast, colorectal, lung, prostate, skin, and stomach malignancies (Yasmin et al. 2023). Additionally, increasing drug resistance in tumor cells emphasizes the necessity of various treatment approaches. Ongoing clinical research into pioneering technologies such as nanomedicines offers promising paths forward. Nanomedicines utilize biocompatible materials for diagnostic and therapeutic purposes, potentially mitigating adverse effects associated with conventional treatments. Reports have highlighted the anticancer potential of medicinal plants and herbal components and revealed that some phytochemicals from these botanicals have the capacity to inhibit cancer cell proliferation, induce apoptosis, inhibit metastasis, and inhibit angiogenesis. HS, which belongs to the Malvaceae family, exhibits promising properties in this field (Pucci et al. 2019). Harnessing the effectiveness of medicinal plants and researching innovative technologies underscore a multifaceted strategy in the fight against cancer. By combining traditional wisdom with contemporary advances, an increasingly optimistic perspective is emerging toward the development of effective and less harmful treatments for this common disease (Desai et al. 2008; Hosseini et al. 2017). There has been some research into the potential anti-cancer properties of hibiscus, particularly in relation to certain cancer cell lines. Hibiscus contains various compounds, such as polyphenols and flavonoids, which have antioxidant properties and may help prevent the growth of cancer cells or induce apoptosis in cancer cells. Studies have shown that hibiscus extracts can inhibit the growth of certain cancer cell lines in vitro, including breast cancer, leukemia, and gastric cancer cell lines. However, more research is needed to fully understand the mechanisms involved and to determine the potential efficacy of hibiscus as a treatment for cancer. It's important to note that while these initial studies are promising, they are mostly preclinical studies done in cell cultures or animal models. Further clinical studies are needed to determine the potential benefits of hibiscus in cancer treatment in humans. Therefore, hibiscus should not be considered a primary treatment for cancer, and its use should always be discussed with a healthcare professional (Lin et al. 2012). Plant extracts have attracted considerable attention in the realm of biosynthetic approaches owing to their safety, widespread availability, and diverse array of metabolites (Amooaghaie et al. 2015; Rehana et al. 2017). Phytochemical constituents like carbohydrates, flavonoids, saponins, proteins, amino acids, and terpenoids present in these extracts play pivotal roles in the synthesis of NPs. Numerous investigations have elucidated the biosynthesis of copper oxide (CuO) NPs utilizing extracts derived from a variety of plant sources including Tinospora cordifolia (Nasrollahzadeh et al. 2015), Carica papaya (Sankar et al. 2014), Tabernaemontana divaricata (Sivaraj et al. 2014), Calotropis gigantea (Sharma et al. 2015), Gloriosa superba (Ghosh et al. 2002), Citrus limon (Prathna et al. 2011), and Hibiscus rosa-sinensis (Gilani et al. 2005). These studies underscore the potential benefits of environmentally benign CuO NPs across diverse biomedical applications. It is noteworthy that conventional chemical synthesis routes for generating CuO NPs and other transition metal oxide NPs have long

been associated with several shortcomings (He et al. 2022; Liu et al. 2024). These drawbacks include substantial energy consumption, environmental contamination, reliance on costly reagents, the necessity for elevated pressure and temperature conditions, and utilization of hazardous chemicals. In this study, we propose that incorporating polyethylene glycol-hibiscus extract-copper (II) oxide nanoparticles (PEG/HS/CuO NPs) into a guar gum photochromic solution (GP) can enhance the multifunctionality of cellulose-based textiles, enabling both screen-printing applications and anticancer therapies. Our goal is to develop a novel PEG/HS/CuO NP formulation that not only imparts visible coloration to cellulose fabrics but also demonstrates selective cytotoxicity against cancer cells, offering a sustainable alternative to conventional textile treatments and potential as a therapeutic strategy for chemotherapy.

Material and method

Chemicals

Dried calyces of HS were obtained from a local supplier in Istanbul, Türkiye, and milled to a particle size of less than 200 µm before extraction. The HS plants were cultivated between November and July of 2021/2022. Guar gum (water-soluble, 99% purity, with an average molecular weight of 2.8×10 g mol^{-1}) was sourced from Fluka (Switzerland). Copper (II) chloride anhydrous (purity 99.995%) and potassium dichromate (K_2CrO_4, ReagentPlus® ≥ 99.5%) were purchased from Sigma Aldrich Company (Germany). Ethanol (purity ≥ 99.5%) and sodium hydroxide were purchased from Merck Company (Germany). All samples were filtered using 0.45 and 0.22-micron retention of sterile syringe filters. The textile used in this study was pure cotton fabric (100 g m^{-2}), purchased from Doğan Çorap Tekstil Sanayi ve Ticaret LTD ŞTİ (Türkiye). All chemicals and reagents were used without further purification.

Preparation of PEG/HS/CuO NPs

The PEG/HS/CuO NPs were synthesized through an economical and environmentally friendly sonication process. Prior to drying in a vacuum oven at 70 °C for 10 h, the powder was thoroughly washed multiple times with distilled water to eliminate any contaminants. The HS was prepared by adding 5.0 g of the dried calyces to 100 mL of distilled water and allowing it to steep at 25 °C in a dark environment for 3 days. Afterward, the solution was filtered through a sterile syringe filter with a retention size of 0.45 microns. To prepare a solution of 1.7 g $CuCl_2$, dissolve it in 250 mL of distilled water. Simultaneously, 0.4 g NaOH was dissolved in 50 mL distilled water. The NaOH solution (4 mL) was gradually mixed into the copper solution, which was then sonicated for 45 min at a frequency of 30% amplitude. Finally, the PEG/HS/CuO NPs were filtered through a sterile syringe filter with a 0.22-micron retention size.

Textile screen-printing application

For the preparation of the PEG/HS/CuO NPs-GG screen-printing nanoformulation, 0.5 g of GG was thoroughly dissolved in 100 mL of distilled water. Subsequently, 10% of a 0.01 mM K_2CrO_4 solution was added, followed by the incorporation of 2 mL of PEG/HS/CuO NPs-GG. This mixture was then thoroughly mixed to create a homogeneous suspension. For the printing process, polyester-based fabrics, measuring 50 cm × 50 cm with approximately 2 mm diameter holes, were prepared (Fig. 1). A suitable shape was prepared for applying the nano-dye (PEG/HS/CuO NPs-GG) before coating the fabric. Finally, the printing process utilized screen printing technology. During the screen printing process, UV light was applied from a height of 25 cm to cure the printed cellulosic fabric. The prepared suspension was applied to cellulose-based textiles using a 100-mesh screen printing technique. The printed cellulosic fabrics were initially dried at 70 °C for 5 min and then baked at 120 °C for 5 min. The process was completed by curing under 300 W UV light for 1–15 min.

Characterization

We employed a range of advanced characterization techniques to analyze the nanostructure, including Transmission Electron Microscopy (TEM) using the Hitachi HighTech HT7700 in high vacuum mode at 100 kV, Fourier Transform Infrared Spectroscopy (FTIR) with the Spectrum Two from Perkin Elmer, utilizing KBr powder within the 4000–400 cm^{-1} frequency range at a resolution of 4 cm^{-1} over 8

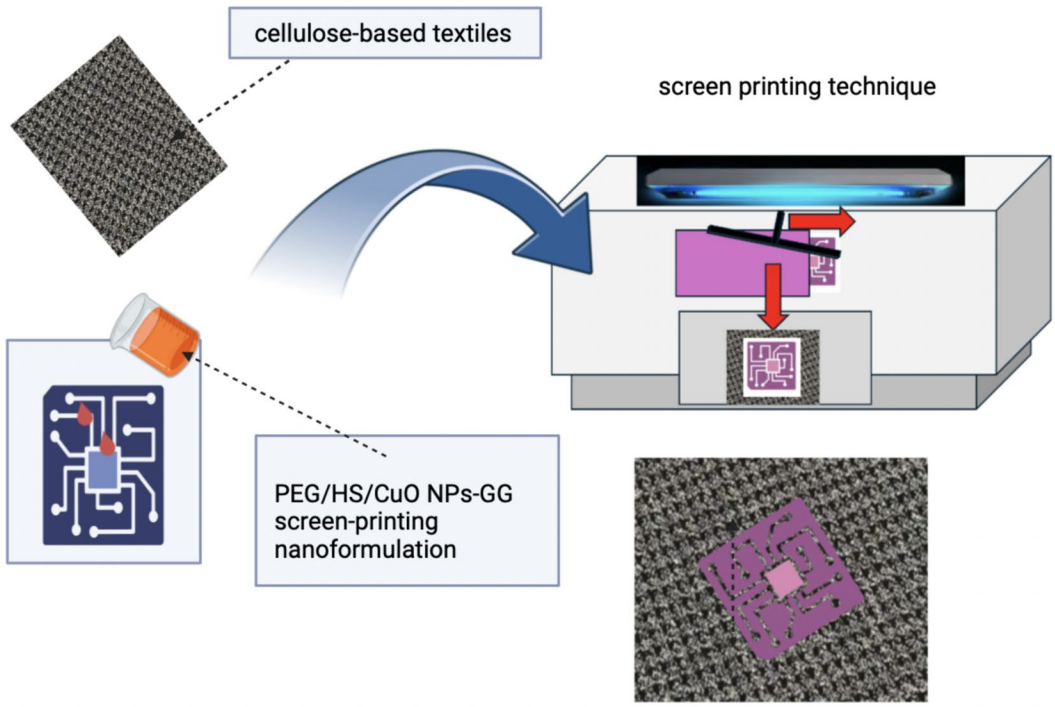

Fig. 1 The schematic diagram of the PEG/HS/CuO NPs-GG nanoformulation process using screen printing technology

scans, and X-ray Diffraction (XRD) utilizing Cu Kα radiation at 40 kV and 15 mA. Scanning electron microscopy (SEM) was performed using the FEI QUANTA 450 instrument, with samples being double-coated with gold to enhance imaging quality. The surface properties of the textile coated with NPs were assessed using SEM–EDX (FEI QUANTA 450) with TedPella double-coating, configured at 8 mmW × 20 mL. To examine the samples' transmission electron microscopy (TEM) images, we used the advanced color analysis software ImageJ 1.51q. This enabled us to quantify and examine structural characteristics and color distribution at a small level. The software supplied extensive insights via digital colorimetric pixel analysis, allowing for a thorough comprehension of the samples' morphology. In addition, we examined images of the samples taken with the Reel Me 12 smartphone before and after screen printing. The Reel Me 12 has a high-resolution 64MP primary camera, a 16MP ultra-wide camera, a 2 MP depth camera, and a 2 MP macro camera. These superior AI-based imaging capabilities meant that the images accurately depicted the samples, which improved our color distribution evaluations. Additionally, the absorbances of the samples were measured using a double-beam UV/Vis spectrophotometer (T + 80, PG Instrument) equipped with UVWin 5 Software.

Cell viability

In this study, we utilized the MCF-7 breast cancer cell line, the HCT116 colon cancer cell line, and HUVEC (human umbilical cord vein endothelial cells) obtained from the American Type Culture Collection (ATCC, MD, USA). These cells were cultured in DMEM supplemented with 10% FBS and 1% penicillin/streptomycin complex plated in cell culture flasks and cultured in a humidified 5% CO_2 incubator at 37 °C. When the cell cultures reached 80–90% confluence, they were passaged, and the growth medium was replaced every 2–3 days. Subsequently, the cells were seeded into 96-well flat-bottom plates at a density of 10^4 cells per well and allowed to adhere for

approximately 2 h. The synthesized HS and PEG/HS/CuO NPs were then added directly to the wells at a 1:1 ratio and further diluted with a medium at ratios of 1:2, 1:4, and 1:8. The cells treated with HS and PEG/HS/CuO NPs were then incubated for 48 h at 37 °C in a humidified atmosphere containing 95% O_2 and 5% CO_2. After the incubation period, 10 µl of 3-(4,5-dimethylthiazol-2-yl)-2,5-diphenyltetrazolium bromide (MTT) solution (5 mg/mL) was added to each well, and the plates were incubated for an additional 4 h. The formazan crystals formed by viable cells were solubilized by adding 100 µL of dimethyl sulfoxide (DMSO), and the absorbance was measured at 570 nm with a reference wavelength of 630 nm using an ELISA reader. Cell viability was calculated as a percentage relative to control wells. The apoptotic cell rate of PEG/HS/CuO NPs on cell lines, their effects on the cell cycle, and the expression of CD44/24 biomarkers were also evaluated. Concentrations of PEG/HS/CuO NPs equivalent to their IC_{50} values were used. After the 48-h incubation period, the cells were analyzed using flow cytometry with Annexin-V/propidium iodide (PI) staining.

Apoptotic activity

Apoptotic activity was determined by Annexin V/PI staining and analyzed by flow cytometry. In order to investigate the apoptotic effects of PEG/HS/CuO NPs, MCF-7 cells were selected due to the high activity of PEG/HS/CuO NPs on cancer cells. The cells were treated with an IC_{50} dose of PEG/HS/CuO NPs for 48 h. Then, cells were stained with 5 µL Annexin V-FITC and 2.5 µL propidium iodide (PI) for 10 min in the dark. Afterward, 400 µL Annexin binding buffer was added, and the processed cells were analyzed by Beckman Coulter Navios flow cytometer (Navios 3L10). Early and late apoptotic cell rates and necrosis rates in these cells were determined by flow cytometry. The data obtained were then analyzed with Kaluza software (Erhardt and Toth 2009; Wlodkowic et al. 2009).

Cell cycle analysis

HCT116 cells were cultured with RL at the IC_{50} concentration for 48 h. After treatment, cells were centrifuged, the supernatant was removed, and the cells were resuspended in PBS. The suspension was then transferred to ethanol for fixation and stored at − 20 °C. Following fixation, cells were washed with PBS, treated with RNase A to remove RNA, and stained with FxCycle™ PI/RNase dye for DNA analysis. Flow cytometry was performed using a Beckman Coulter Navios system, and the data were analyzed with Kaluza Analysis Software to assess cell cycle distribution.

CD44 and CD24

The cell lines were analyzed for their apoptotic activity and cell cycle phase distribution in their original state. The CD44 and CD24 antibodies were incubated for a period of 15–20 min in the dark at room temperature. The isotypic control antibodies were employed as a reference standard, as were the fluorescent properties of the cells themselves. Following a single wash with PBS, the cells were analyzed using flow cytometry with the Beckman Coulter Navios instrument and the Kaluza analysis program. The optimal wavelengths for compatibility were found to be between 488 and 561 nm, with an emission at 578 nm. A minimum of 10,000–15,000 cells were analyzed for each tube.

Results and dıscussıon

Characterization of the NPs

Figure 2 presents the TEM images of PEG/HS/CuO NPs at magnifications of × 40.0 k and × 120.0 k. The experimental results clearly demonstrated that the PEG/HS/CuO NPs exhibited an irregular morphology, with diameters consistently below 20 nm. This small size suggested a large surface area for the nanostructures, and they generally showed a good distribution. However, some partial agglomeration was observed among the particles, although it was minimal. These findings highlighted the effectiveness of the sonochemical synthesis method in producing NPs with controlled size distribution and minimal clustering.

Figure 3 presents a detailed analysis of PEG/HS/CuO NPs using various TEM imaging techniques. In Fig. 3a, the AI-supported TEM image, rendered in an 8-bit rainbow color scale, enhanced contrast and clarity, making the boundaries and morphology

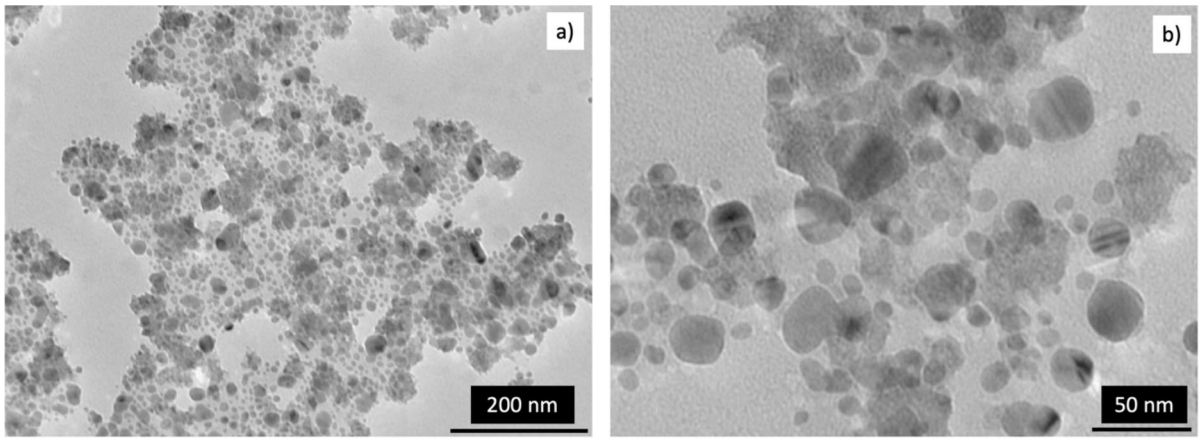

Fig. 2 **a** TEM image of PEG/HS/CuO NPs with × 40.0 k and × 120.0 k

of the PEG/HS/CuO NPs more distinct. ImageJ 1.51q software was utilized for this analysis, and the TEM images were first converted to an 8-bit format for image processing. The green color highlighted the uniform distribution of the PEG/HS/CuO NPs, while the blue color indicated areas of partial agglomeration. Notably, most of the structure (over 95%) appeared in green, providing evidence of the homogenous distribution and successful synthesis of the PEG/HS/CuO NPs. Figure 3b presents the TEM image's topographic map (isoline), providing detailed insights into the surface characteristics and depth variations of the PEG/HS/CuO NPs. The relatively minor elevation differences suggested an overall smooth surface; however, approximately 70% of the image displayed sharp partial peaks, indicating the presence of free particles and a certain degree of inhomogeneity. Additionally, broad flat areas, constituting around 30% of the surface, were observed, contributing to the partial agglomeration of the PEG/HS/CuO NPs. This combination of features highlighted the complex topography of the NPs, accentuating both the uniform regions and those with more intricate textures. Furthermore, these analytical techniques underscored the significance of artificial intelligence in microscopic analysis, particularly when investigating extremely small nanostructures, revealing intricate details that enhance our understanding of their morphology and distribution. Figure 3c–d illustrates the color distribution and histogram of the TEM image, with the corresponding colors positioned 50 nm beneath the overall distribution of PEG/HS/CuO NPs. Collectively, these photos offered visual evidence, considerably supported by AI, of the NPs' shape, distribution, and surface properties, confirming the quality of their manufacture. Furthermore, these analytical tools demonstrated the importance of AI in microscopic analysis, particularly when studying extremely small nanostructures, exposing complex characteristics that help us comprehend their form and distribution.

Fig. S1 presents the FTIR spectra of (a) HS and (b) PEG/HS/CuO NPs. These spectra highlight the distinct functional groups and molecular interactions in the extract (HS) compared to the PEG/HS/CuO NPs, showcasing the changes in chemical bonding and surface modifications after NPs synthesis. The FTIR spectra for HS revealed several characteristic peaks, including 3329 cm^{-1}, corresponding to OH stretching, 2917 cm^{-1} for symmetric C–H stretching, 2848 cm^{-1} for asymmetric C–H stretching, 1726 cm^{-1} for C = O stretching, 1615 cm^{-1} for protein amide I, 1185 cm^{-1} for antisymmetric C–O stretching, and 1013 cm^{-1} for C–O–C stretching (Fig. S1a). In comparison, the spectra for PEG/HS/CuO NPs exhibited peaks at 3329 cm^{-1} (OH stretching), 1596 cm^{-1} (symmetric C-H stretching), 1374 cm^{-1} (asymmetric C-H stretching), 1224 cm^{-1} (C=O stretching), and 1067 cm^{-1} (C–O stretching) shifts indicate interactions between the extract and metal ions (Fig. S1b) (Ramli and Nair 2015). A weak band at 883 cm^{-1} indicated the presence of a glycosidic linkage, while a peak at 673 cm^{-1} corresponded to the formation and stretching of CuO. The significant peaks observed at 3329 cm^{-1}, 1650 cm^{-1}, 1482 cm^{-1}, and 883 cm^{-1} in both the

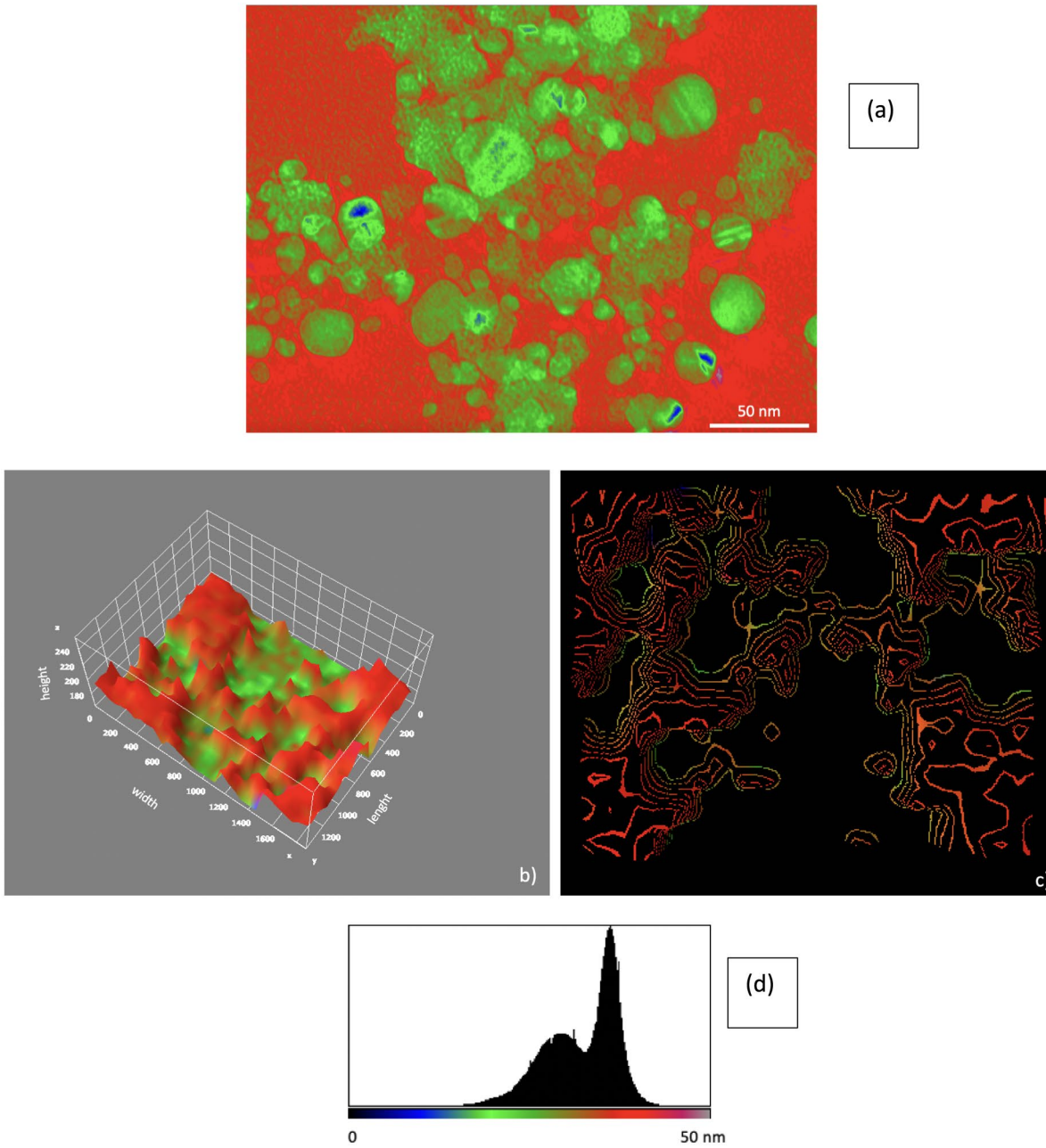

Fig. 3 **a** AI-enhanced TEM image of PEG/HS/CuO NPs (8-bit rainbow scale), **b** topographic map of the TEM image of PEG/HS/CuO NPs (isoline representation), **c** color distribution graph of the AI-enhanced TEM image of PEG/HS/CuO NPs, and **d** corresponding color histogram

extract and CuO NPs spectra confirmed the presence of bio-based molecules on the surface of the NPs. The bending vibrations of υ(Cu–O–H) were considered responsible for the minor peak at 883 cm^{-1} (Ananda Murthy et al. 2021). The XRD graph of the prepared PEG/HS/CuO NPs is given in Fig. S2. The XRD results revealed distinct diffraction peaks for PEG/HS/CuO NPs at 2θ values of 28°, 32°, 40°, 45°,

47°, 56°, and 75° are indexed to (110), (002), (111), (200), (202), (311), (222) planes of monoclinic CuO as referenced against JCPDS Card No. 04–015-5865.

Figure 4a–e depicts the following: (a) SEM image of the uncoated cellulose-based material, (b) SEM image of the cellulose-based material coated with NPs after screen printing, (c) AI-enhanced SEM image of the NPs rendered in 8-bit rainbow-smart mode, and (d) SEM–EDX mapping of the cellulose-based material coated with NPs, showing (e) the elemental distribution of carbon (C), copper (Cu), and sulfur (S). The AI-supported imaging enhanced contrast and clarity, allowing for a detailed examination of the NPs' morphology and their distribution on the substrate. The SEM image of uncoated cellulose-based textiles showed a smooth, well-defined and flat surface (Fig. 4a). The SEM image of the cellulose-based textiles coated with PEG/HS/CuO NPs revealed a uniform layer with partially agglomerated nanostructures, demonstrating the effective distribution and adhesion of the NPs across the textile surface (Fig. 4b). Furthermore, it was observed in these images that the textile coated with PEG/HS/CuO NPs contained a layered structure covered with small NPs (red/yellow color reflections) (Fig. 4c). The SEM–EDX results for the cellulose-based material coated with PEG/HS/CuO NPs after screen printing revealed the presence of essential constituent elements of the NPs, including carbon (C), oxygen (O), and sulfur (S), along with copper (Cu) from the PEG/HS/CuO NPs-GG sample (Fig. 4d–e). These experimental results revealed that PEG/HS/CuO NPs-GG were successfully dispersed on cellulose-based textile and formed a homogeneous coating.

These structural and surface characterizations align with the synthesis mechanism of PEG/HS/CuO NPs. The sonosynthesis of PEG/HS/CuO NPs using ultrasonic irradiation leverages the localized high temperatures and pressures generated by ultrasonic waves. These extreme conditions facilitate the rapid nucleation of CuO NPs. Plant extract serves as both a reducing and stabilizing agent, while PEG functions as a capping agent, crucially controlling the size and morphology of the NPs while preventing aggregation. The synthesis process involves a series of chemical reactions driven by the interaction of system components. Copper(II) ions (Cu^{2+}) from the precursor solution are reduced by phenolic compounds and flavonoids present in the extract, which donate electrons to convert Cu^{2+} to Cu^{+} and subsequently to CuO NPs. Although forming the CuO phase at 10 °C is typically challenging due to the dehydration and oxidation reactions requiring temperatures above 60 °C, a sonochemical approach enables the synthesis of CuO NPs at 25 °C. The mechanism of CuO NPs formation under these conditions is outlined as follows (Kim et al. 2016):

$$Cu^{2+} + 2OH^{-} \rightarrow Cu(OH)^{2} \quad (1)$$

$$Cu(OH)_2 + 2OH^{-} \rightarrow [Cu(OH)_4]^{2-} \quad (2)$$

$$[Cu(OH)_4]^{2-} \rightarrow CuO + 2OH^{-} + H_2O \quad (3)$$

Screen printing of textile coated with PEG/HS/CuO NPs into the GP solution

The incorporation of NPs in screen printing materials plays a critical role in enhancing the functional properties of printed surfaces. For example, as reported by Chakkarapani et al. (Chakkarapani et al. 2024), NPs such as silver and reduced graphene oxide have been effectively used to modify carbon screen printing electrodes, enabling selective and sensitive determination of phenolic compounds. This highlights how NPs can increase the performance of printed materials, especially in applications that need precision, sensitivity, and conductivity, making them invaluable in advanced technologies like as detectors and electrochemical instruments. Similarly, (Yang et al. 2022) reported the preparation of high-performance flexible planar micro-supercapacitors through screen printing, using MoS_2 NPs decorated with electrochemically exfoliated graphene. From a different perspective, (Meshram et al. 2017) demonstrated how anti-microbial surfaces can be developed by depositing ZnO NPs on PVA-gelatine composite films using the screen printing technique. This approach not only improved the antimicrobial activity but also contributed to the overall biological compatibility of the material. To achieve the photochromic effect, screen printing was employed to coat cellulose-based textiles with multifunctional NPs. This method has proven to be fast, user-friendly, cost-effective, and easily repeatable, effectively showcasing the functional, biological, surface, and chemical properties of textile

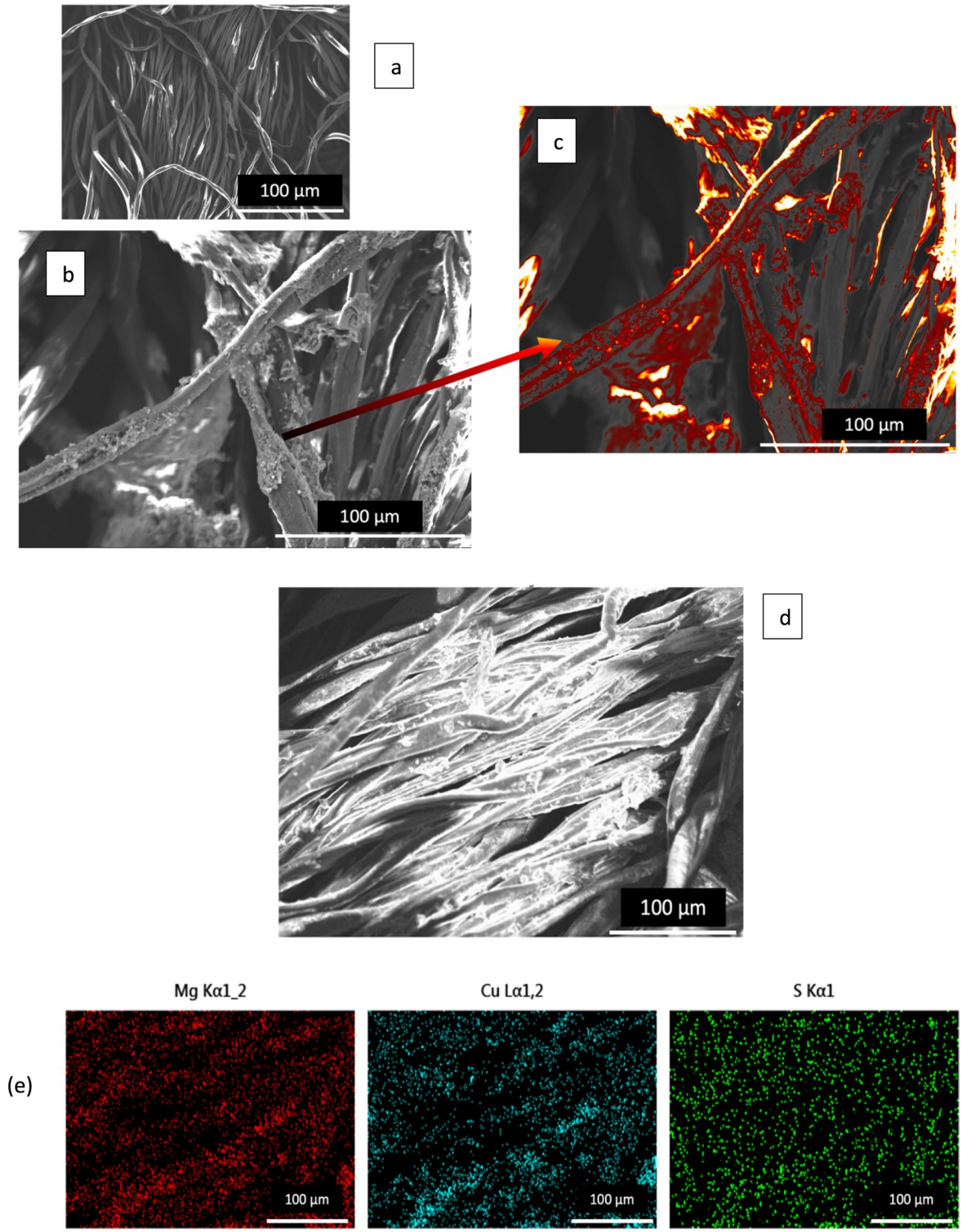

Fig. 4 (**a**) SEM image of the uncoated cellulose-based material, (**b**) SEM image of the cellulose-based material coated with NPs after screen printing, (**c**) AI-enhanced SEM image of the NPs rendered in 8-bit rainbow-smart mode, and (**d**) SEM–EDX mapping of the cellulose-based material coated with NPs, showing (**e**) the elemental distribution of carbon (C), copper (Cu), and sulfur (S)

materials. Moreover, screen printing offers promising applications in wearable bio-based sensors, providing a practical means of integrating advanced functionalities into textiles while preserving their flexibility and usability. In this study, cellulosic fabrics were coated with bio-based NPs and cured under 300 W UV light for various durations (curing times: 1–15 min). To assess the impact of the GG biopolymer on printing quality, curing times of PEG/HS/CuO NPs were tested both in the presence and absence of GG, with three replicates for each condition. The inclusion of GG enhanced printing quality by improving the adhesion of NPs to the fabric surface. This enhancement occurred because GG facilitates a more uniform distribution and better adhesion of the bio-ink, creating a superior film during the printing process. The effects of PEG/HS/CuO NPs-GG on printing quality and coating performance were meticulously evaluated. In Fig. 5a–e, the following images are given: (a) photograph of polyester and cellulosic fabrics coated with PEG/HS/CuO NPs, (b) PEG/HS/CuO-GG NPs, (c) cellulosic fabrics after screen printing with PEG/HS/CuO-GG NPs, (d) PEG/HS/CuO NPs cured under UV light for 6 ± 1 min, and (e) PEG/HS/CuO NPs after 6 ± 1 min curing. In Fig. 5f–g, the addition of GG during the screen printing process significantly improved the uniformity of the color distribution, as seen in the color histograms. Specifically, the color histogram in (Fig. 5f), which represents the structure cured with PEG/HS/CuO NPs without GG, displays a narrower range, indicating less variation in color distribution. On the other hand, the histogram in (Fig. 5g), showing the results for PEG/HS/CuO-GG NPs, presents a broader, more evenly spread graph. This suggests that the presence of GG promotes a more uniform distribution of NPs on the fabric, enhancing overall coverage and producing a more homogenous color distribution. In conclusion, the optimal condition was found to be a curing time of 6 ± 1 min in the presence of PEG/HS/CuO-GG NPs, based on three replicates per experiment. This condition resulted in more uniform color distribution and more effective NP coating, leading to superior printing and coating performance.

Cell cytotoxicity

Extracts from the HS, containing organic acids, protocatechuic acid, anthocyanins, citric acids, flavonoids, saponins, tannins, caffeic acids, polyphenols, and various other compounds, have been documented to possess anti-cancer properties. These constituents have demonstrated abilities to decrease cancer cell proliferation, trigger apoptosis, and induce cell cycle arrest. In this investigation, we explored the cytotoxic effects of HS and PEG/HS/CuO NPs on MCF-7 breast cancer, HCT116 colon cancer, and HUVEC normal cells (Fig. 6a–f). Our results revealed significant cytotoxicity of HS on both MCF-7 and HUVEC cells. However, HS demonstrated enhanced cytotoxicity in HCT116 cells relative to the control group. Moreover, it is notable that the cytotoxicity was further induced when treated with PEG/HS/CuO NPs across all groups. Furthermore, the highest toxicity was observed for HS and PEG/HS/CuO NPs on MCF-7 cells among all cell groups. Furthermore, the viability of HUVEC cells treated with HS was found to be lower than that of HCT116 cells, but higher than that of MCF-7 cells. In MCF-7 cells, undiluted HS (1:4 ratio) resulted in approximately half of the cells dying, a result that was comparable to that observed with PEG/HS/CuO NPs at the same dilution. This indicates that the PEG/HS/CuO NPs were four times more cytotoxic than HS. Conversely, HS exhibited low cytotoxicity on HUVEC cells, while PEG/HS/CuO NPs caused approximately 32% cell death at a dilution ratio of 1:4 and approximately 50% cell death at a dilution of 1:2. When the cytotoxicity of PEG/HS/CuO NPs was compared between HUVEC and MCF-7 cells, a dilution ratio of 1:4 resulted in approximately 50% cell death in MCF-7 cells, while 32% of HUVEC cells died, indicating a lower level of toxicity in normal cells. In summary, PEG/HS/CuO NPs demonstrated higher cytotoxicity against MCF-7 cancer cells compared to HUVEC normal cells. A comparison of the cytotoxicity of PEG/HS/CuO NPs on HUVEC and MCF-7 cells revealed that the former exhibited a higher degree of toxicity, with approximately half of the MCF-7 cells undergoing death at a dilution ratio of 1:4, whereas the latter demonstrated a lower level of cell death, with approximately 32% of cells dying at the same concentration. Previous studies by Christopher Nguyen and colleagues have demonstrated the efficacy of HE in inducing apoptosis in both triple-negative MDA-MB-231 and ER + MCF-7 breast cancer cells (Nguyen et al. 2019). The other study reported that HE has been shown to induce apoptosis significantly around treatment of 2 mg/

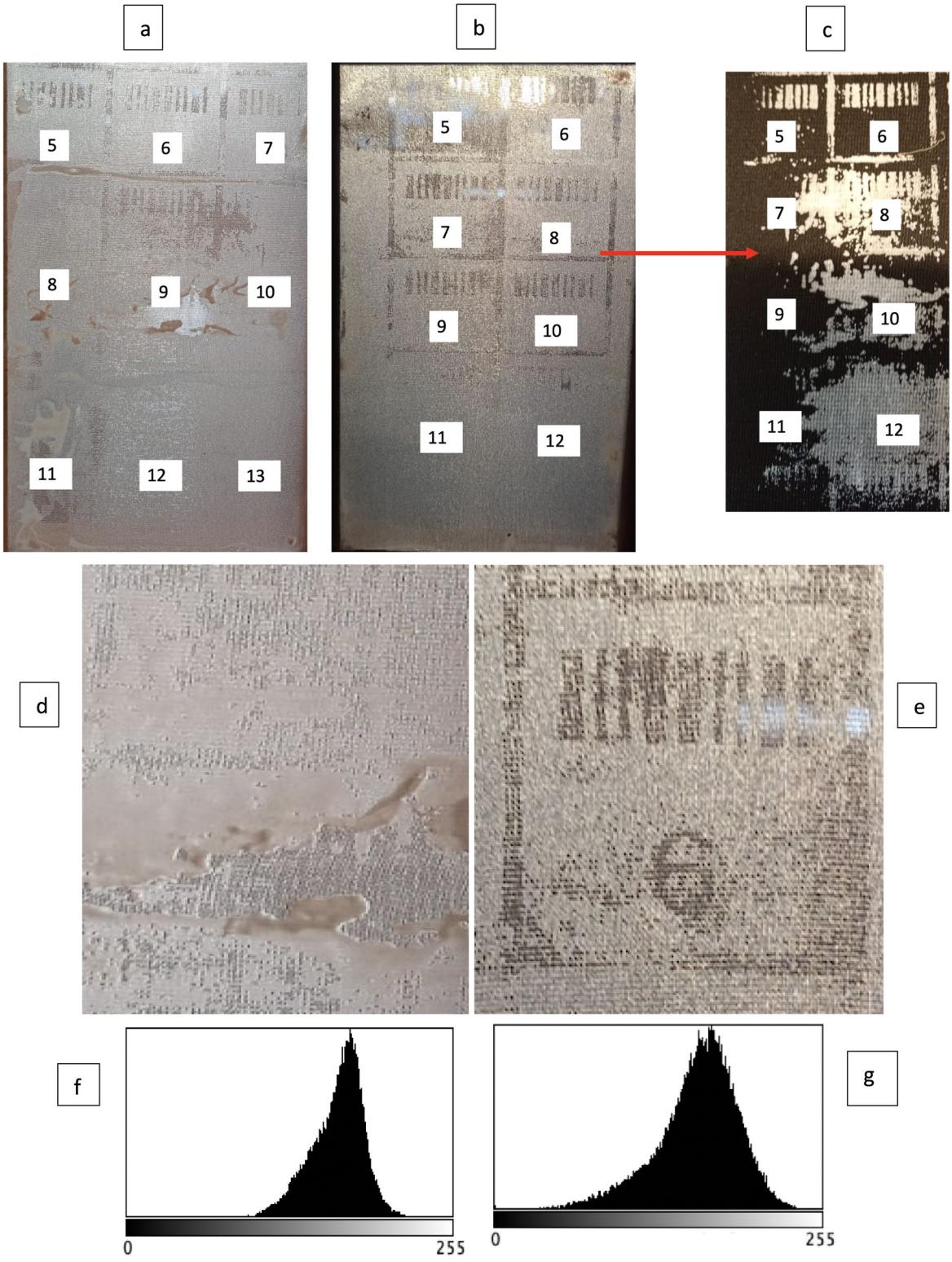
a
b
c
5
6
7
8
9
10
11
12
13
d
e
f
g
0
255
0
255

◂**Fig. 5** **a** Photograph of polyester and cellulosic fabrics coated with PEG/HS/CuO NPs; **b** PEG/HS/CuO-GG NPs; **c** cellulosic fabrics after screen printing with PEG/HS/CuO-GG NPs; **d** PEG/HS/CuO NPs cured under UV light for 6 ± 1 min; **e** PEG/HS/CuO NPs after 6 ± 1 min curing; **f** color histogram of the structure cured with PEG/HS/CuO NPs; and **g** PEG/HS/CuO-GG NPs

mL of crude extract in prostate cancer, with a similar dose-dependency (Chiu et al. 2015). Thun et al. have reported findings indicating that the HS, applied at a dose of 4 mg/mL for 48 h in vitro conditions on breast cancer cell lines, induced apoptosis and increased ROS and mitochondrial membrane collapse (Thun et al. 2010). In our study, PEG/HS/CuO NPs clearly showed selectivity by increasing cytotoxicity in cancer cells. In addition, in Table 1, brief summaries of NPs prepared by different studies are given and compared with our study.

Apoptosis, also known as programmed cell death, is a fundamental process necessary for maintaining morphogenetic homeostasis during early development and in various pathophysiological conditions. Multiple studies have identified the dysregulation of various apoptotic components during the development and progression of cancer. Apoptosis depends on the activation of specific signaling pathways, which are frequently disrupted in cancer (Kashyap et al. 2021). As illustrated in Fig. 7 of our study, PEG/HS/CuO NPs have been demonstrated to induce cell death by apoptosis.

The present study was conducted on the MCF7 cell line with the objective of evaluating changes in the CD44 + /CD24− cancer stem cell (CSC) populations, which are associated with drug resistance and metastasis.Treatment with CuO NPs reduced the CD44 + /CD24− population from 29.68 to 8.43%, while the CD44-/CD24- population increased from 70.28 to 91.54%. (Fig. 8). These findings suggest that CuO NPs effectively reduce proliferation, migration, and metastatic potential, highlighting their role in combating drug resistance and tumorigenic activity.

In our study, we also investigated the effects of PEG/HS/CuO NPs on the cell cycle in MCF-7 cancer cells. Consistent with the findings of Liu et al. (2017), who showed that GTPs induce cell cycle arrest at G1/M and G2/M checkpoints while promoting apoptosis, our results revealed significant changes in cell cycle dynamics following treatment with PEG/HS/CuO NPs (Liu et al. 2017). In particular, we observed that the G0/G1 phase increased from 50.17% in control cells to 59.52% after treatment, indicating a shift towards cell cycle arrest and growth arrest. This was accompanied by a significant decrease in the S phase, indicating that DNA synthesis and overall cell growth were effectively inhibited. Furthermore, the decrease in G2/M phase activity reinforces the idea that PEG/HS/CuO NPs exert strong inhibitory effects on cell proliferation (Fig. 9). In a similar study, Simsek et al. (2020) found that carbon-based NPs caused an arrest in the G0/G1 phase on MCF-7 cells, resulting in a transition to the S phase and inhibition of cell growth. That is, they detected a significant increase in the G0/G1 population with a significant decrease in both S and G2/M phases (Şimşek et al. 2020). In summary, our findings emphasize the potential of these agents to improve cancer therapy by specifically inducing cell cycle arrest and apoptosis.

Conclusion

In conclusion, the dual-functional PEG/HS/CuO NPs showed substantial promise for biological and material-related applications. Their specific cytotoxicity against cancer cells, notably MCF-7 breast cancer cells, along with their capacity to cause G2/M phase cell cycle arrest and apoptosis make them intriguing chemotherapeutic options. The synthesized PEG/HS/CuO NPs exhibited an irregular morphology with sizes below 20 nm, enhancing their ability to establish effective contact with biological cells. Furthermore, these PEG/HS/CuO NPs were successfully mixed into a photochromic GG for screen printing onto cellulose-based textiles, presenting a novel method for creating smart materials. A curing time of 6 ± 1 min under UV light was found to be optimal for screen printing, with GG playing a key role in ensuring uniform distribution and strong adherence of NPs to the textile surface. This study offers promising avenues

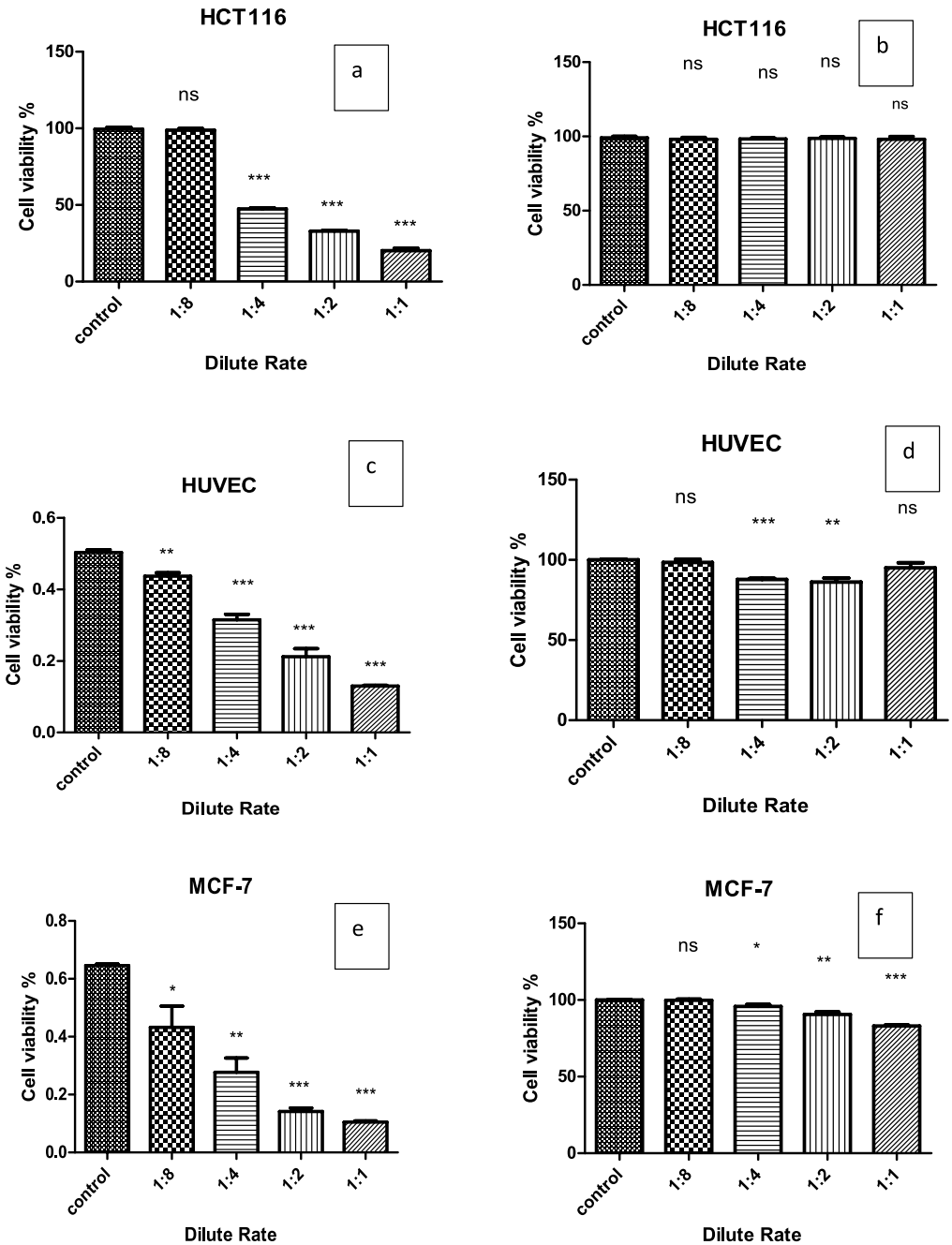

Fig. 6 The concentrations depicted in the graph were applied using HB to assess cytotoxicity. For HCT-116, various concentrations of PEG/HS/CuO NPs (**a**) and HS (**b**) were applied by diluting them as 1/8, 1/4, 1/2, and 1. The impact of PEG/HS/CuO NPs was assessed in graph (**c**), while HS was evaluated in graphs (**d**) on HUVEC cells. Additionally, the effects of PEG/HS/CuO NPs (**e**) and HS (**f**) on MCF-7 cells are presented in the graph. Statistical significance was indicated by $p < 0.001$ (***), and $p < 0.01$ (**) when compared to the control group. The samples were analyzed using the Student-*t* test. Statistical analysis was performed using GraphPad Prism 8.0 (GraphPad Software, San Diego, CA). Each test was conducted at least three times

Table 1 Comparison of the different NPs in different areas

Treatment	Size	Results	Refs
PEG-coated Cu@Se nano-hybrid	~ 109 nm	Potential anticancer activity, DU145, LNCaP cells	(Liu et al. 2020)
Cobalt oxide (Co_3O_4-NPs), magnesium oxide nanoparticles (MgO–NPs)	~28–19 nm	Multiple biomedical applications	(Kainat et al. 2021)
AuNPs-Hibiscus, AuNPs-Curcumin	~ 20 nm	Potential anticancer, HCT116, MCF-7	(Liu et al. 2020)
AgNPs and HS leaf extract	21.22 nm	Antibacterial and anticancer activity, A549	(Ahirwar et al. 2024)
ZnO, Au, and Au/ZnO NPs	50.7, 51.6, 8.45 nm	Anticancer activity, MCF-7	(Shochah and Jabir 2024)
PEG/HS/CuO NPs	less than 20 nm,	For biological and material-related applications, MCF-7, HCT116, HUVEC	This study

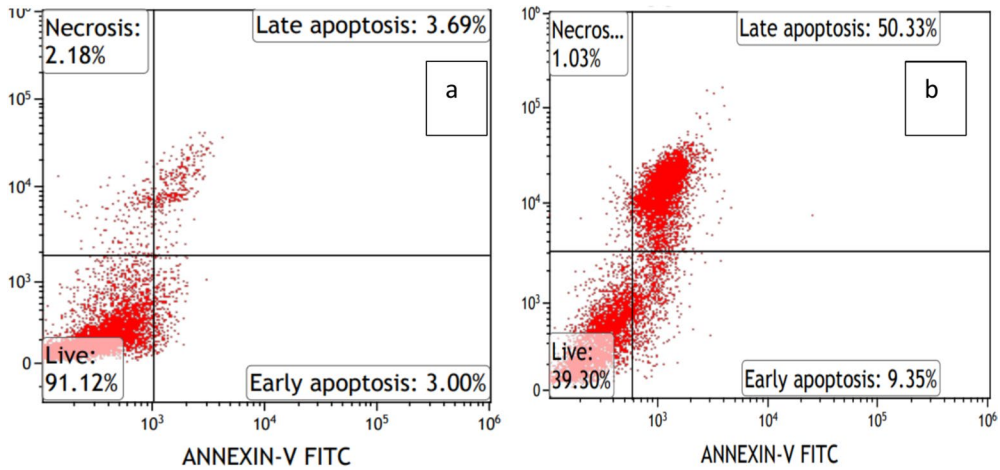

Fig. 7 The apoptotic effects of HS and PEG/HS/CuO NPs in MCF-7 cells. (a) MCF-7 cells treated with HS (b) MCF-7 cells treated with PEG/HS/CuO NPs at IC_{50} values

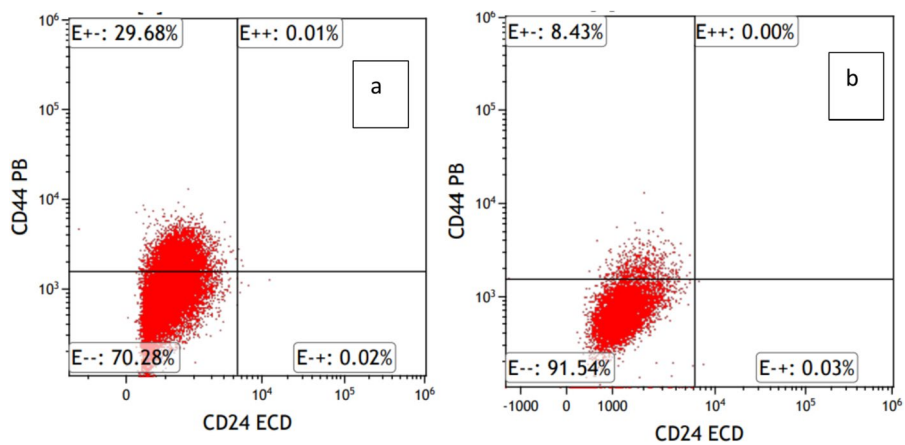

Fig. 8 CD44 + /CD24- cell surface marker analysis by flow cytometry. The graph illustrates the percentage of cells treated with HS and PEG/HS/CuO NPs at the IC_{50} value. (a) MCF-7 cells treated with HS, (b) MCF-7 cells treated with PEG/HS/CuO NPs

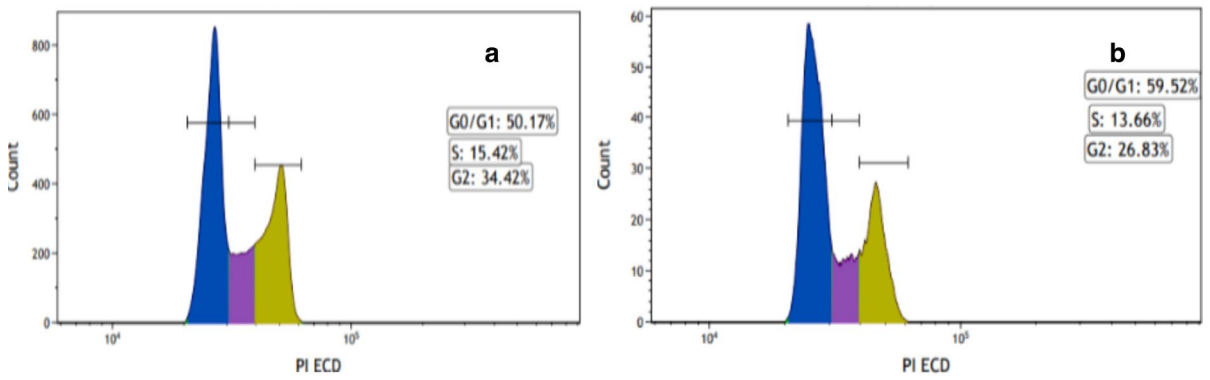

Fig. 9 The graph illustrates the percentage of cells in the cell cycle phase treated with HS and HS-CuO at the IC_{50} value. (**a**) Untreated MCF-7 cells, (**b**) MCF-7 cells treated with HS-CuO NPs

for future research into the application of these nanostructures in anticancer therapies and multifunctional smart materials, particularly in wearable sensor technologies and advanced textiles.

Acknowledgments The authors acknowledge the financial support by Researchers Supporting Project number (RSP2025R79) at King Saud University, Riyadh, Saudi Arabia.

Author contributions Elif Tüzün; investigation; writing—review and editing. Ayşe Erol: formal analysis. Ferdane Danışman Kalındemirtaş: formal analysis, writing—review and editing. Razium Ali Soomro: writing—review, and editing. Ayman Nafady: writing—review and editing. Fatih Özbaş: formal analysis. Esra Sert: formal analysis. Selcan Karakuş: supervision; conceptualization; writing—review and editing.

Funding Open access funding provided by the Scientific and Technological Research Council of Türkiye (TÜBİTAK). This work was supported by the Scientific Research Projects Coordination Unit of Istanbul University. Project number: 40437.

Data availability Not applicable.

Declarations

Conflict of interest The authors declare no conflict of interest.

Ethical approval Not applicable.

Consent to participate Not applicable.

Consent for publication All the authors consent for the publication of this article.

References

Ahirwar B, Ahirwar D, Jain R et al (2024) Biofabricated green synthesized hibiscus silver nanoparticles potentiate antibacterial activity and cytotoxicity in human lung cancer cells. Appl Biochem Biotechnol. https://doi.org/10.1007/S12010-024-04901-X/TABLES/4

Alsharief HH, Al-Hazmi GAA, Alzahrani SO et al (2022) Immobilization of strontium aluminate nanoparticles onto plasma-pretreated nonwoven polypropylene fibers by screen-printing toward photochromic textiles. J Market Res 20:3146–3157. https://doi.org/10.1016/J.JMRT.2022.08.104

Amooaghaie R, Saeri MR, Azizi M (2015) Synthesis, characterization and biocompatibility of silver nanoparticles synthesized from Nigella sativa leaf extract in comparison with chemical silver nanoparticles. Ecotoxicol Environ Saf 120:400–408. https://doi.org/10.1016/J.ECOENV.2015.06.025

Ananda Murthy HC, Zeleke TD, Tan KB et al (2021) Enhanced multifunctionality of CuO nanoparticles synthesized using aqueous leaf extract of Vernonia amygdalina plant. Results Chem 3:100141. https://doi.org/10.1016/J.RECHEM.2021.100141

Andra S, Balu S, Jeevanandam J et al (2021) Surface cationization of cellulose to enhance durable antibacterial finish in

phytosynthesized silver nanoparticle treated cotton fabric. Cellulose 28:5895–5910. https://doi.org/10.1007/S10570-021-03846-2/TABLES/2

Chakkarapani LD, Bytešníková Z, Richtera L, Brandl M (2024) Selective and sensitive determination of phenolic compounds using carbon screen printing electrodes modified with reduced graphene oxide and silver nanoparticles. Appl Mater Today 37:102113. https://doi.org/10.1016/J.APMT.2024.102113

Chiu CT, Chen JH, Chou FP, Lin HH (2015) *Hibiscus sabdariffa* leaf extract inhibits human prostate cancer cell invasion via down-regulation of Akt/NF-kB/MMP-9 Pathway. Nutrients 7:5065–5087. https://doi.org/10.3390/NU7075065

Desai AG, Qazi GN, Ganju RK et al (2008) Medicinal plants and cancer chemoprevention. Curr Drug Metab 9:581. https://doi.org/10.2174/138920008785821657

dos Santos VF, Fontana LC, Missner MEP et al (2023) Study on functional properties of cotton fabrics using an environmentally friendly deposition of TiO_2 nanoparticles. Cellulose 30:5407–5417. https://doi.org/10.1007/s10570-023-05211-x

Erhardt P, Toth A (eds) (2009) Apoptosis. p 559. https://doi.org/10.1007/978-1-60327-017-5

Ghosh B, Mukherjee S, Jha TB, Jha S (2002) Enhanced colchicine production in root cultures of Gloriosa superba by direct and indirect precursors of the biosynthetic pathway. Biotechnol Lett 24:231–234. https://doi.org/10.1023/A:1014129225583/METRICS

Gilani AH, Bashir S, Janbaz KH, Shah AJ (2005) Presence of cholinergic and calcium channel blocking activities explains the traditional use of Hibiscus rosasinensis in constipation and diarrhoea. J Ethnopharmacol 102:289–294. https://doi.org/10.1016/J.JEP.2005.07.023

He X, Kim H, Dong TG et al (2022) Green synthesis of Ag/lignin nanoparticle-loaded cellulose aerogel for catalytic degradation and antimicrobial applications. Cellulose 29:9341–9360. https://doi.org/10.1007/S10570-022-04848-4/TABLES/2

Hosseini A, Bakhtiari E, Mousavi SH (2017) Protective effect of *Hibiscus Sabdariffa* on doxorubicin-induced cytotoxicity in H_9c_2 cardiomyoblast cells. Iran J Pharm Res 16:708

Hu H, Shang S, Liu J, Zhu P (2024) Silk fibroin based flexible and self-powered sensor for real-time monitoring of abdominal respiration. Int J Biol Macromol 254:127723. https://doi.org/10.1016/J.IJBIOMAC.2023.127723

Kainat KMA, Ali F et al (2021) Exploring the therapeutic potential of Hibiscus rosa sinensis synthesized cobalt oxide (Co_3O_4-NPs) and magnesium oxide nanoparticles (MgO–NPs). Saudi J Biol Sci 28:5157–5167. https://doi.org/10.1016/J.SJBS.2021.05.035

Kashyap D, Garg VK, Goel N (2021) Intrinsic and extrinsic pathways of apoptosis: role in cancer development and prognosis. Adv Protein Chem Struct Biol 125:73–120. https://doi.org/10.1016/BS.APCSB.2021.01.003

Kim DS, Kim JC, Kim BK, Kim DW (2016) One-pot low-temperature sonochemical synthesis of CuO nanostructures and their electrochemical properties. Ceram Int 42:19454–19460. https://doi.org/10.1016/J.CERAMINT.2016.09.044

Lin HH, Chan KC, Sheu JY et al (2012) Hibiscus sabdariffa leaf induces apoptosis of human prostate cancer cells in vitro and in vivo. Food Chem 132:880–891. https://doi.org/10.1016/J.FOODCHEM.2011.11.057

Liu SM, Ou SY, Huang HH (2017) Green tea polyphenols induce cell death in breast cancer MCF-7 cells through induction of cell cycle arrest and mitochondrial-mediated apoptosis. J Zhejiang Univ Sci B 18:89–98. https://doi.org/10.1631/JZUS.B1600022/METRICS

Liu Y, Guo Q, Sun H et al (2020) Improved therapeutic efficiency of photothermal treatment and nursing care in prostate cancer by DOX loaded PEG coated Cu@Se nanohybrid vesicle. Process Biochem 92:78–84. https://doi.org/10.1016/J.PROCBIO.2020.02.022

Liu JL, Qu LY, Shi YL et al (2024) Fabrication of antimicrobial viscose fibers containing silver nanoparticle@catechol formaldehyde resin microspheres. Cellulose 31:703–715. https://doi.org/10.1007/S10570-023-05647-1/FIGURES/8

Marques Mandaji C, da Silva PR, Campos Chisté R (2022) Encapsulation of bioactive compounds extracted from plants of genus Hibiscus: a review of selected techniques and applications. Food Res Int 151:110820. https://doi.org/10.1016/J.FOODRES.2021.110820

Marra F, Minutillo S, Tamburrano A, Sarto MS (2021) Production and characterization of Graphene Nanoplatelet-based ink for smart textile strain sensors via screen printing technique. Mater des 198:109306. https://doi.org/10.1016/J.MATDES.2020.109306

Meshram JV, Koli VB, Phadatare MR, Pawar SH (2017) Antimicrobial surfaces: an approach for deposition of ZnO nanoparticles on PVA-Gelatin composite film by screen printing technique. Mater Sci Eng, C 73:257–266. https://doi.org/10.1016/J.MSEC.2016.12.043

Nasrollahzadeh M, Maham M, Mohammad Sajadi S (2015) Green synthesis of CuO nanoparticles by aqueous extract of Gundelia tournefortii and evaluation of their catalytic activity for the synthesis of N-monosubstituted ureas and reduction of 4-nitrophenol. J Coll Interface Sci 455:245–253. https://doi.org/10.1016/J.JCIS.2015.05.045

Nguyen C, Baskaran K, Pupulin A et al (2019) Hibiscus flower extract selectively induces apoptosis in breast cancer cells and positively interacts with common chemotherapeutics. BMC Complement Altern Med. https://doi.org/10.1186/S12906-019-2505-9

Prathna TC, Chandrasekaran N, Raichur AM, Mukherjee A (2011) Biomimetic synthesis of silver nanoparticles by Citrus limon (lemon) aqueous extract and theoretical prediction of particle size. Colloids Surf B Biointerfaces 82:152–159. https://doi.org/10.1016/J.COLSURFB.2010.08.036

Pucci C, Martinelli C, Ciofani G (2019) Innovative approaches for cancer treatment: current perspectives and new challenges. Ecancermedicalscience. https://doi.org/10.3332/ECANCER.2019.961

Ramli S, Nair G (2015) Optical characterization using nature based dye extracted from hibiscus's flower MHz on rats female reproductive system physiology view project dielectric measurement view project Muhammad Irwanto

Rehana D, Mahendiran D, Kumar RS, Rahiman AK (2017) Evaluation of antioxidant and anticancer activity of copper oxide nanoparticles synthesized using medicinally

important plant extracts. Biomed Pharmacother 89:1067–1077. https://doi.org/10.1016/J.BIOPHA.2017.02.101

Riaz G, Chopra R (2018) A review on phytochemistry and therapeutic uses of *Hibiscus sabdariffa* L. Biomed Pharmacother 102:575–586. https://doi.org/10.1016/J.BIOPHA.2018.03.023

Sankar R, Manikandan P, Malarvizhi V et al (2014) Green synthesis of colloidal copper oxide nanoparticles using Carica papaya and its application in photocatalytic dye degradation. Spectrochim Acta A Mol Biomol Spectrosc 121:746–750. https://doi.org/10.1016/J.SAA.2013.12.020

Shahzadi N, Yousaf MI, Ashraf M (2024) Room temperature stimulated long-persistent phosphorescence of polyurethane/$SrAl_2O_4$: Eu^{2+}, Dy^{3+} composite material for textile-based applications. Ceram Int. https://doi.org/10.1016/J.CERAMINT.2024.08.394

Sharma JK, Akhtar MS, Ameen S et al (2015) Green synthesis of CuO nanoparticles with leaf extract of Calotropis gigantea and its dye-sensitized solar cells applications. J Alloys Compd 632:321–325. https://doi.org/10.1016/J.JALLCOM.2015.01.172

Shochah QR, Jabir FA (2024) Green synthesis of Au/ZnO nanoparticles for anticancer activity and oxidative stress against MCF-7 cell lines. Biomass Convers Biorefin 14:15283–15296. https://doi.org/10.1007/S13399-022-03697-2/TABLES/2

Şimşek S, Şüküroğlu AA, Yetkin D et al (2020) (2020) DNA-damage and cell cycle arrest initiated anti-cancer potency of super tiny carbon dots on MCF7 cell line. Sci Rep 10(1):1–14. https://doi.org/10.1038/s41598-020-70796-3

Sivaraj R, Rahman PKSM, Rajiv P et al (2014) Biogenic copper oxide nanoparticles synthesis using Tabernaemontana divaricate leaf extract and its antibacterial activity against urinary tract pathogen. Spectrochim Acta A Mol Biomol Spectrosc 133:178–181. https://doi.org/10.1016/J.SAA.2014.05.048

Thun MJ, DeLancey JO, Center MM et al (2010) The global burden of cancer: priorities for prevention. Carcinogenesis 31:100–110. https://doi.org/10.1093/CARCIN/BGP263

Wan J, Li H, Xu L et al (2023) PDA/PEI-induced in-situ growth of a lotus leaf-like TiO_2 nanoparticle film on N-halamine cotton fabric for photocatalytic, self-cleaning and efficient antibacterial performance. Cellulose 30:3953–3972. https://doi.org/10.1007/s10570-023-05088-w

Wlodkowic D, Skommer J, Darzynkiewicz Z (2009) Flow cytometry-based apoptosis detection. Methods Mol Biol 559:19–32. https://doi.org/10.1007/978-1-60327-017-5_2

Yang W, Hu Z, Zhang C et al (2022) Screen printing preparation of high-performance flexible planar micro-supercapacitors based on MoS_2 nanoparticles decorated electrochemically exfoliated graphene. Electrochim Acta 429:141041. https://doi.org/10.1016/J.ELECTACTA.2022.141041

Yasmin R, Gogoi S, Bora J et al (2023) Novel Insight into the cellular and molecular signalling pathways on cancer preventing effects of *Hibiscus sabdariffa*: a review. J Cancer Prev 28:77. https://doi.org/10.15430/JCP.2023.28.3.77

Zhang K, Shang S, Zheng Y et al (2024) Biobased multifunctional Poly(lactic acid) nanofiber membranes for efficient personal thermal management. ACS Appl Polym Mater 6:1389–1399. https://doi.org/10.1021/ACSAPM.3C02516/SUPPL_FILE/AP3C02516_SI_001.PDF

Zheng Y, Lin G, Zhou W et al (2024) Bioinspired polydopamine modification for ınterface compatibility of PDMS-based responsive structurally colored textiles. ACS Appl Mater Interfaces. https://doi.org/10.1021/ACSAMI.4C11967